Computational Assessment and Evolution of MQ1-Predator Design

Abdullah Saleh Refaat, Abdulrahman Elazazi Mohamed, Mohamed Ahmed Mohamed, Mohamed Samir Abdelmonem, Roba Tarek AbdelFatah, and Shawky Mohamed Mohamed
Zagazig University, Egypt, abdoallahsaleh14@gmail.com, abdelrahman.elazazy2001@gmail.com, mohameddahmed1112@gmail.com, mohammedsamir9630@gmail.com, roba.tarek.laptop@gmail.com, shawky123.sk80@gmail.com
Supervisors: Prof. Dr. Ahmed Farouk AbdelGawad, Chair of Mechanical Power Engineering Department
Dr. Amr Ahmed Zamel, Computer Engineering and Systems Department
Zagazig University, Egypt, afaroukgb@gmail.com, eng.amrzml@gmail.com

Abstract*– This study concerns the evaluation and development of the performance of MQ-1 Predator airplane from the aspects of design, and manufacturing. Based on the design and aerodynamic performance aspects, the computational models were developed by ANSYS-Fluent software to determine the aerodynamic characteristics of the baseline design and to study modifications applied to the design to achieve the optimum design and performance. The pressure and velocity contours of the wing model and the whole aircraft model are demonstrated at different angles of attack to show the flow characteristics and the stall effects. The coefficients of lift and drag were determined against different angles of attack. Finally, the manufacturing phase included a scaled model of the modified aircraft. The model has all the required assumptions and considerations for surface roughness, and model kinematics and balance using carbon fiber with wooden, and metal supports to be a lightweight model with suitable structure, which can withstand the loads.

Keywords-- MQ-1 Predator, Computational investigation, Experimental model, Carbon fiber UAV.

I. Introduction

National security of any country is affected by various factors, which recently have been considered by possessing the unmanned aerial vehicles (UAVs). They are totally preferable over the manned ones as they can work in dull, dirty, and dangerous environment. Such advantages attract anyone in this field to study the common ones especially the long service-life aircrafts [1]. In 2012, MQ-1 Predator, as a distinctive UAV, was described as one of the most accident-prone aircraft in the USA Air Force fleet [2].

Various CFD studies have been applied to investigate the behavior of unmanned aircrafts. In 2010, Sweeten studied three different UAVs (YAK-54, the Manta Hawk, and the Meridian) using different software and high fidelity CFD [3]. Zhen *et al.* studied the aerodynamic performance of the Aludra UAV [4]. In 2014, Krishnamurthy *et al.* investigated a UAV wing design, and applied modifications on the wing geometry and studied the influence of minute changes on flow characteristics of the airplane. Different aerodynamic characteristics, such as lift, drag, stall angle, and lift-to-drag ratio of each wing, were determined [5].

Prakash *et al.* implemented CFD studies and external geometrical modifications to MQ-1 Predator UCAV. They found that, when applying modifications, the aerodynamic characteristics changed as the lift dropped and the drag increased due to these modifications. Also, they stated that it is needed to choose suitable locations of the external modifications to get better aerodynamic performance [6].

All previous studies have focused on how the external modifications affect the aerodynamic performance of the aircraft. However, CFD provides an effective alternative and can help to study and analyze the effects of the external modifications in an efficient, yet accurate manner. Due to the lack of computational and experimental studies on the MQ-1 Predator, Figure1, the present study focuses on studying the baseline aircraft, and then applying modifications of adding slots to the wing and comparing the change in the aerodynamic performance.

Fig. 1. MQ-1 Predator [7].

II. Computational Aspects

Governing Equations

The simulation is governed by the continuity, Navier-Stokes (momentum conservation), and energy equations. For the turbulent flow, the Reynolds-Averaged version of these equations was used. The Spalart-Allmaras turbulence model was used to close the Reynolds-Averaged equation set. The Spalart-Allmaras turbulence model has been developed for aerospace applications that are wall-bounded and subject to adverse pressure gradients. The Spalart-Allmaras model has only one equation, which solves for the kinematic eddy viscosity. The variables of the problem are solved in all cell centers of the mesh. In total, there are six variables to solve for: three components of velocity, pressure, temperature, and the

kinematic eddy viscosity. The equations are given as follows [8], [9], [10]:

- Continuity Equation: $\frac{\partial \rho}{\partial t} + \frac{\partial}{\partial t}(\rho u_i) = 0$ (1)
- Raynold's -Averaged Navier-Stokes Equation:

$$\rho\left(\frac{\partial U_i}{\partial t} + \frac{\partial}{\partial x_i}(U_i U_j)\right) = -\frac{\partial P}{\partial x_i} + \frac{\partial}{\partial x_i}\left(2\mu S_{ij} - \rho\underline{u_i' u_j'}\right) \quad (2)$$

- Conservation of Energy Equation:

$$\frac{\partial}{\partial t}(\rho e_o) + \frac{\partial}{\partial x_i}\left[\rho u_j e_o + u_j p + q_j - u_j T_{ij}\right] = 0 \quad (3)$$

- Spalart-Allmaras Turbulence Model $\overline{u_i' u_j'} = 2\upsilon_T S_{ij}$ (4)

General Considerations

ANSYS-Fluent R18.2 was used for the steady-state solution of the incompressible turbulent flow with the energy model. Spalart-Allmaras one-equation turbulence model was adopted. The fluid properties and boundary conditions were determined by using an online program by NASA [11].

The lift and drag coefficients were plotted at different angles of attack for different cases of both the baseline and the modified designs. The stall angle was determined for each case. The inclined slot was added to the wing of MQ-1 Predator to test its aerodynamic effectiveness on the stall angle. The velocity and pressure distributions were demonstrated along and around the MQ-1 Predator.

III. Simulation Setup for Different Case Studies

Different operating conditions (cases) were conducted to determine the stall of MQ-1 Predator, its behavior, and examine the effect of adding inclined slots to the wing.

CAD Modeling

Without any available geometry provided by the designer of MQ-1 Predator and depending on the drawings shown in Figure. 2, professionals provided 3D CAD model of the whole aircraft with full system payload in GrabCAD. Some issues have been faced with this model such as gaps, interferences, zero thickness features, and multiple parts. These problems were fixed, obtaining the shown CAD model in Fig. 3. Then, all the models of the case studies and domains were constructed out of this baseline model to have the four following models, based on the similarity of the two halves of the MQ-1 Predator:

1- Baseline half-wing model.
2- Modified half-wing model.
3- Baseline half-aircraft model
4- Modified half-aircraft model

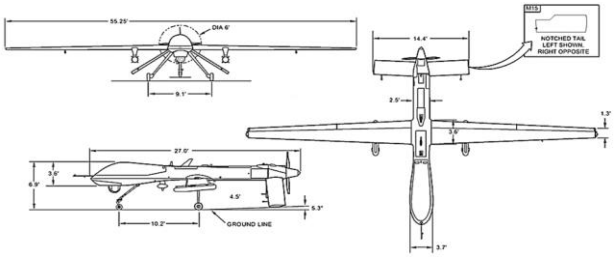

Fig. 2. MQ-1 Predator projected views [12].

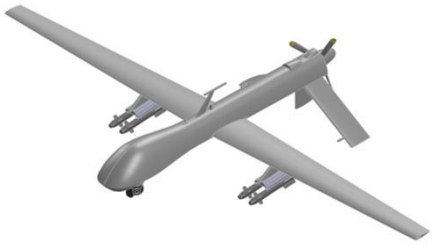

Fig. 3. GrabCAD 3D Model [13].

Baseline half-wing model

Based on the aircraft drawings and fixed GrabCAD model, SolidWorks 2018 software was used to construct the present baseline wing model to perform the baseline case studies. The present baseline wing model is shown in Fig. 4. The computational domain was built in ANSYS-Fluent Design Modeler as a box enclosure with the specifications clarified in Table I and shown in Fig. 5. The named selections for these cases are shown in Fig. 6.

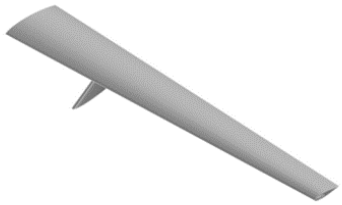

Fig. 4. Baseline case of half-wing model.

TABLE I
BASELINE HALF-WING DOMAIN SPECIFICATIONS

Shape	Ratio to chord length
+X value	15
+Y value	20
+Z value	30
-X value	15
-Y value	25
-Z value	60

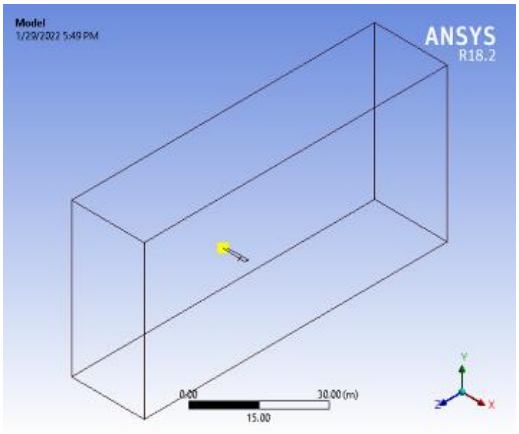

Fig. 5. Computational Domain of baseline case of half-wing model.

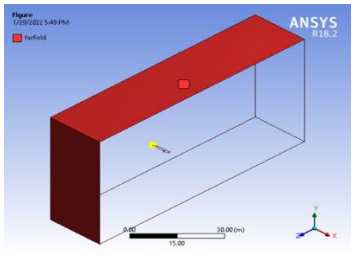

(a)

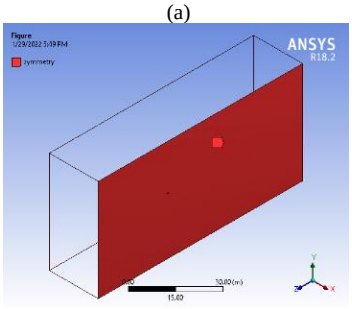

(b)

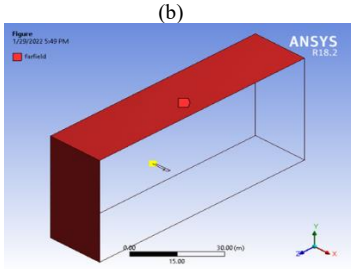

(c)

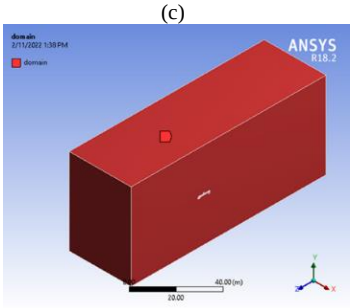

(d)

Fig. 6. Domain terminology (Named Selection): (a) farfield, (b) symmetry, (c) wing, (d) domain.

Modified half-wing model

The present modification is based on making a slot in the wing to optimize the aerodynamic design of the aircraft. Three inclined slots at 30, 45, and 60° were applied. It was located at 16.7% of the chordline with thickness of 5 mm as shown in Fig. 7. The domain was built in ANSYS-Fluent Design Modeler as a box enclosure with the similar specifications to baseline half-wing model.

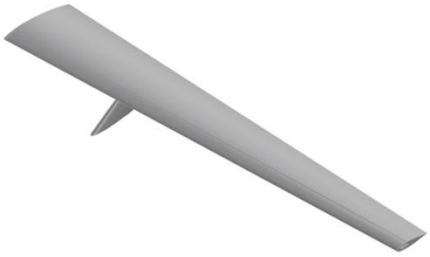

Fig. 7. Slotted half-wing model.

Baseline half-aircraft model

Based on the aircraft drawings and fixed GrabCAD model, SolidWorks 2018 software was used for the present baseline aircraft model to perform the baseline case studies. The present baseline aircraft model is shown in Fig. 8. The domain was built in ANSYS-Fluent Design Modeler as a box enclosure with the specifications clarified in Table II and shown in Fig. 9. The named selections for these cases are shown in Fig. 10.

Fig. 8. Baseline case of half-aircraft model.

TABLE II
BASELINE HALF-AIRCRAFT DOMAIN SPECIFICATIONS

Shape	Ratio to chord length
+X value	30
+Y value	25
+Z value	40
-X value	30
-Y value	25
-Z value	70

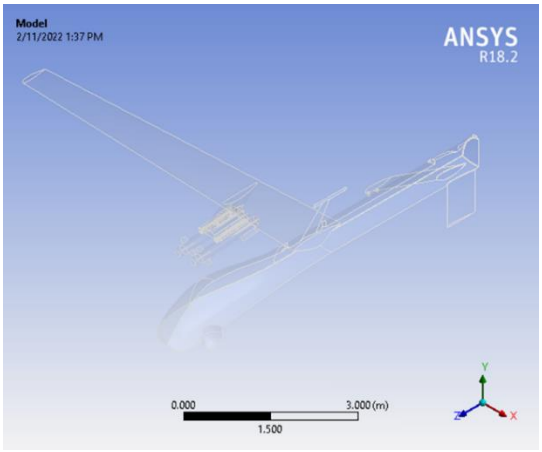

Fig. 9. Baseline case of half-aircraft model.

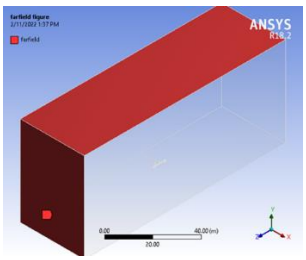

(a)

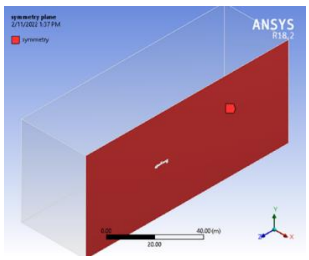

(b)

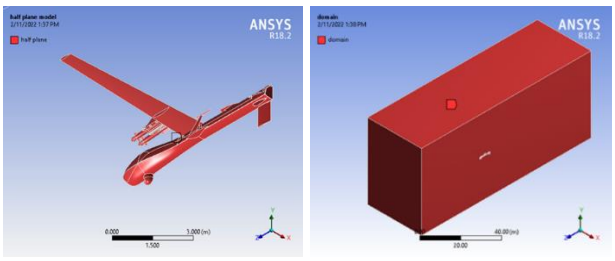

(c) (d)

Fig. 10. Domain terminology (Named Selection): (a) farfield, (b) symmetry, (c) aircraft, (d) domain.

Modified half-aircraft model

The present modification, that was applied to the wing only, was applied to the wing attached to the aircraft in addition to its weapon system by making a slot in the wing to optimize the aerodynamic design of the aircraft as shown in Fig. 11. The domain was built in ANSYS-Fluent Design Modeler as a box enclosure with the similar specifications to baseline half-aircraft model.

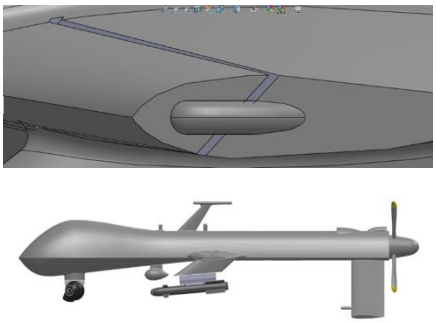

Fig. 11. Slotted half-aircraft model.

Computational Mesh

The second step, after preparing the CAD model with the proper domain, is to mesh the model. For the present case studies, there were four mesh configurations:

1- Baseline half-wing model mesh.
2- Modified half-wing model mesh.
3- Baseline half-aircraft model mesh
4- Modified half-aircraft model mesh

For the four models, the mesh is fine with face sizing on the half-wing surface of 0.005 m element size and 5 inflation layers with first layer thickness of 0.0001 m and growth rate 1.2 at the half-wing surface.

Baseline half-wing model mesh

The mesh is shown in Fig. 12. The general specifications of the mesh are shown in Table III.

TABLE III
BASELINE HALF-WING MESH SPECIFICATIONS

Object Name	Mesh	
Statistics		
Nodes	5,040,696	
Elements	18,375,466	
Face sizing		
Scope		
Named selection	Wing	Domain
Type	Element size	
Element size	5×10^{-3} m	
Inflation		
Boundary scoping method		Named selection
Boundary		Wing
Inflation option		First layer thickness
First layer height		1×10^{-4} m
Maximum layers		5
Growth rate		1.2

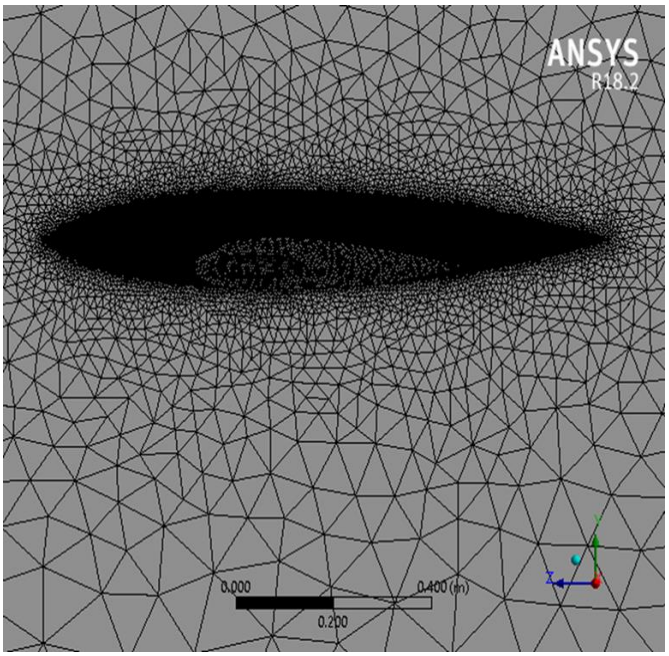

Fig. 12. Baseline half-wing at high altitude face sizing.

Modified half-wing model mesh

The mesh is shown in Fig. 13. The general specifications of the mesh are shown in Table IV.

TABLE IV
MODIFIED HALF-WING MESH SPECIFICATIONS

Object Name	Mesh	
Statistics		
Nodes	5,627,950	
Elements	20,175,586	
Face sizing		
Scope		
Scoping Method	Named selection	
Named selection	Wing	Domain
Definition		
Type	Element size	
Element size	5×10^{-3} m	
Boundary scoping method		Named selection
Boundary		Wing
Inflation option		First layer thickness
First layer height		1×10^{-4} m
Maximum layers		5

Growth rate		1.2

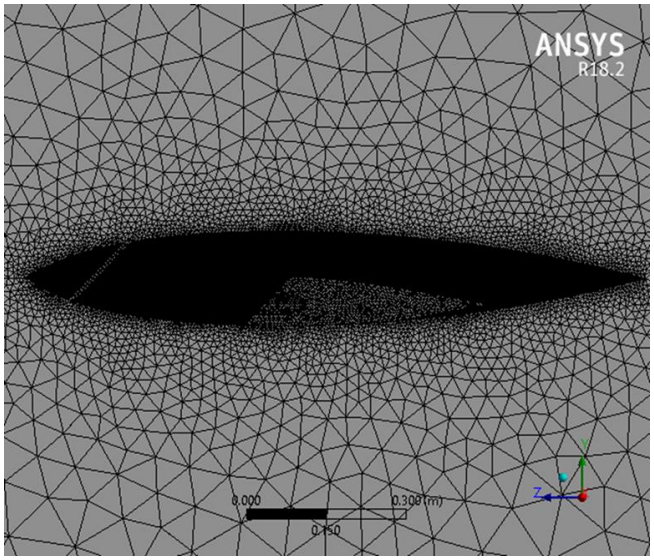

Fig. 13. Modified half-wing face sizing.

Baseline half-aircraft model mesh

The mesh is shown in Fig. 14. The general specifications of the mesh are shown in TABLE V.

TABLE V
BASELINE HALF-AIRCRAFT MESH SPECIFICATIONS

Object Name	Mesh	
Statistics		
Nodes	12,680,700	
Elements	46,802,411	
Face sizing		
Scope		
Named selection	Half plane	Domain
Type	Element size	
Element size	5×10^{-3} m	
Inflation		
Boundary scoping method		Named selection
Boundary		Half plane
Inflation option		First layer thickness
First layer height		1×10^{-4} m
Maximum layers		5
Growth rate		1.2

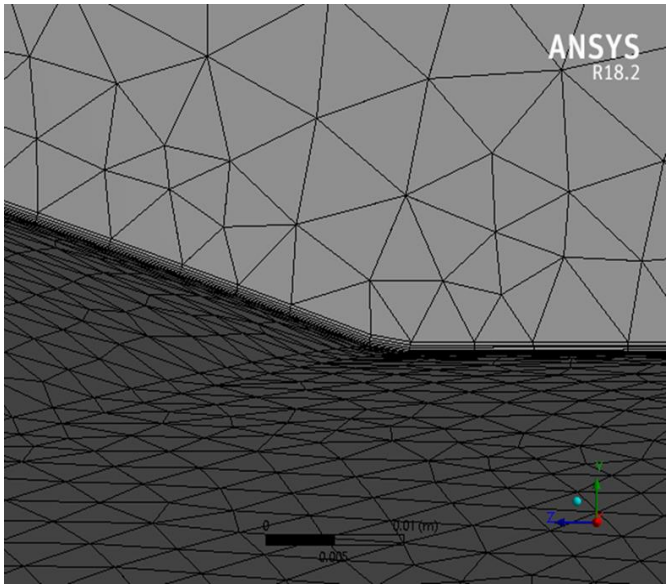

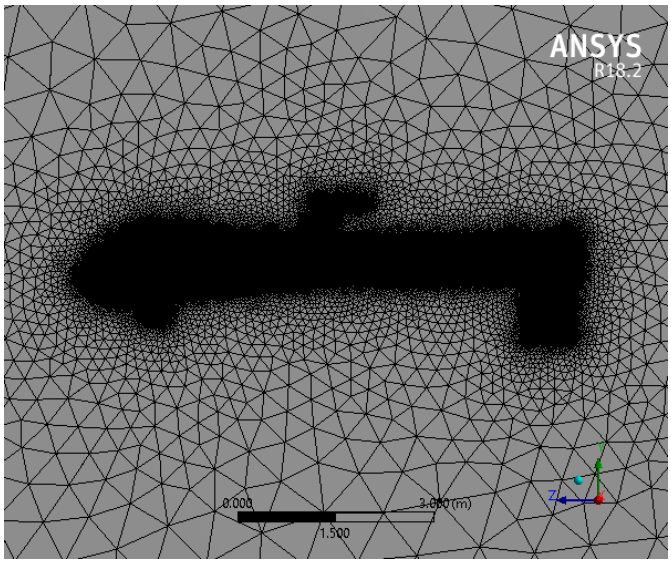

Fig. 14. Baseline half-aircraft at high altitude face sizing.

Modified half-aircraft model mesh

The mesh is shown in Fig. 15. The general specifications of the mesh are shown in Table VI.

TABLE VI
MODIFIED HALF-AIRCRAFT MESH SPECIFICATIONS

Object Name	Mesh	
Statistics		
Nodes	12,885,732	
Elements	46,510,296	
Face sizing		
Scope		
Scoping Method	Named selection	
Named selection	Half plane	Domain
Definition		
Type	Element size	
Element size	5×10^{-3} m	
Boundary scoping method		Named selection
Boundary		Half plane
Inflation option		First layer thickness

First layer height		1×10^{-4} m
Maximum layers		5
Growth rate		1.2

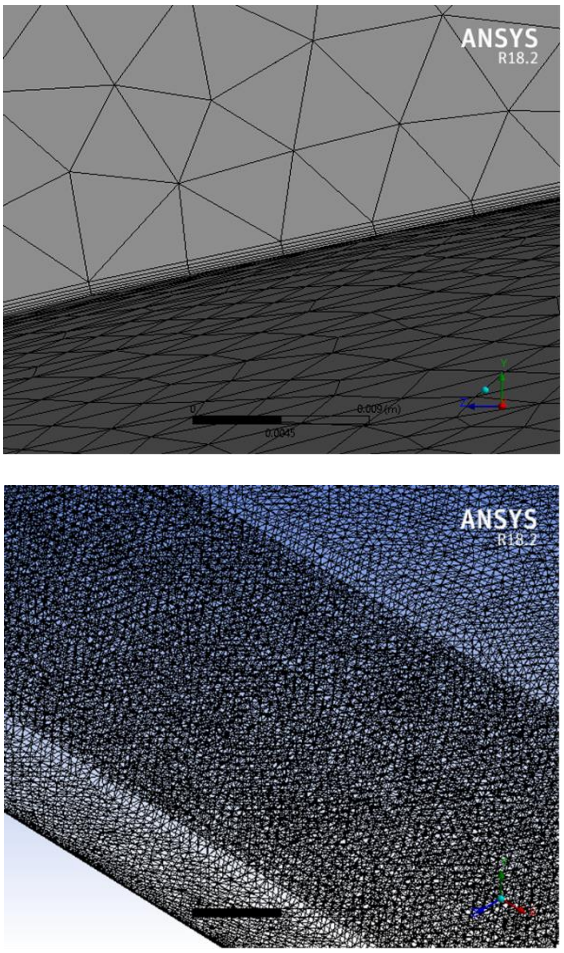

Fig. 15. Modified half-aircraft face sizing.

Solution Setup

For both the baseline and modified cases, the air is taken as ideal gas flowing at 47.2 m/s (170 km/h) at a height of 7,600 m. The type of boundary conditions used in this case are pressure farfield to the sides of the domain except the plane of symmetry of the wing, which has a symmetry boundary condition. More details are shown in Table VII.

TABLE VII
SETUP INPUTS OF THE BASELINE HALF-WING AT HIGH-ALTITUDE FLIGHT

Angle of Attack (AoA) α (°)	**Projected Area (m^2)**	**Air kinematic viscosity ($N.s/m^2$)**	**Temperature (K)**	**Operation Pressure (kPa)**	**Mach number (M)**
0	0.95773	1.4938×10^{-5}	239	37.728	0.152
1	0.97611				
2	0.98283				
3	1.01362				
4	1.01257				
5	1.04666				
6	1.08104				
7	1.11491				
8	1.15802				
9	1.22348				
10	1.28380				
11	1.35484				
12	1.44191				
13	1.51148				

III. RESULTS AND DISCUSSIONS

Baseline half-wing model

The solution of this case appeared not to be stable at the angle of attack 14°, which appeared to be the stall angle. Table VIII shows the results obtained by the baseline half-wing model at high altitude flight case. Figures 16 and 17 show the pressure contours and velocity streamlines at mid-section of the wing at angles of attack 2° and 13°, respectively.

TABLE VIII
BASELINE HALF-WING MODEL AT HIGH-ALTITUDE FLIGHT RESULTS

AoA (α)°	**Projected area (m^2)**	**Lift coefficient c_l**	**Drag coefficient c_d**
0	0.95773	-0.03619	0.08402
1	0.97611	0.46900	0.08308
2	0.98283	0.95099	0.08711
3	1.01362	1.34010	0.09364
4	1.01257	1.71690	0.10670
5	1.04666	1.97481	0.12015
6	1.08104	2.15610	0.13847
7	1.11491	2.26320	0.16539
8	1.15802	2.37010	0.20555
9	1.22348	2.64330	0.27239
10	1.28380	2.97600	0.35309
11	1.35484	3.25570	0.43338
12	1.44191	3.50920	0.54455
13	1.51148	3.89660	0.72650
14	1.59632	Stall	

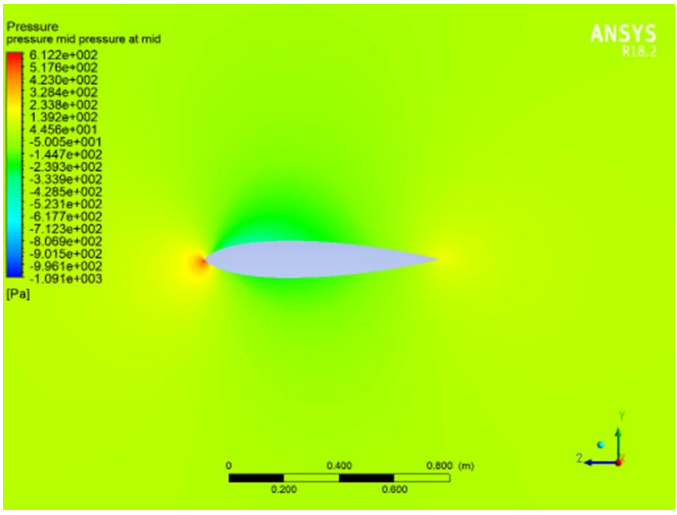

(a)

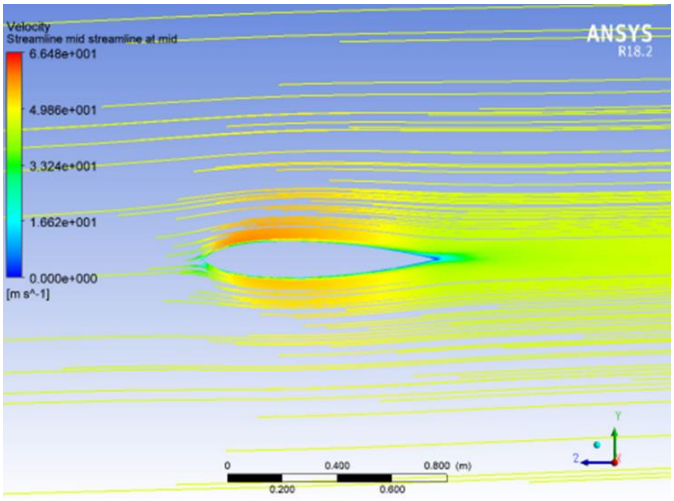

(b)

Fig. 16. Mid-section at α = 2°, (a) pressure contours (b) velocity streamlines.

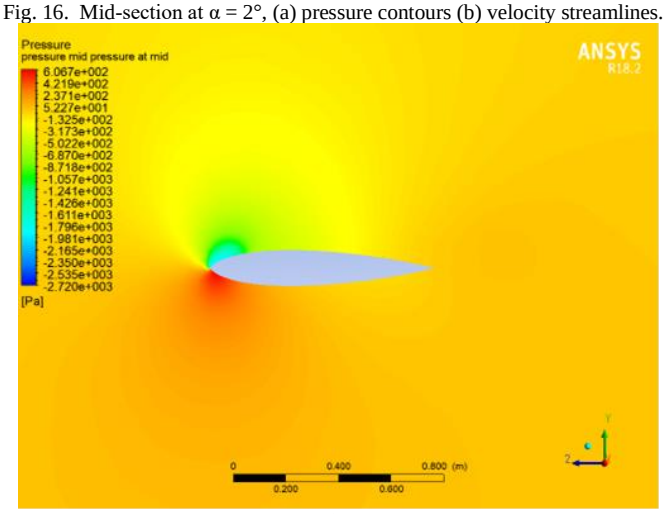

(a)

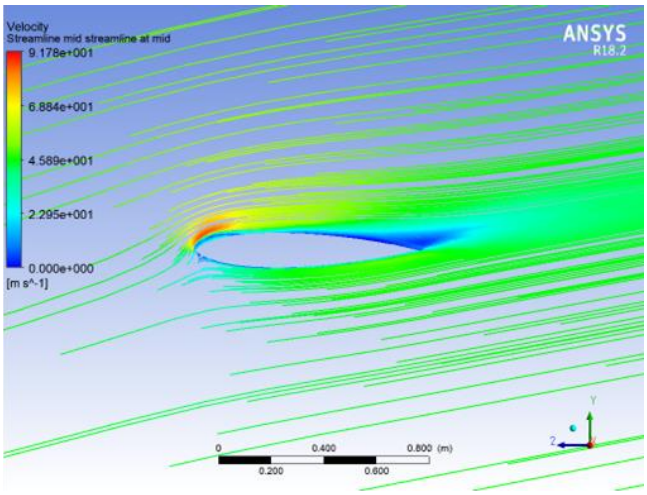

(b)

Fig. 17. Mid-section at α =13°, (a) pressure contours (b) velocity streamlines.

Modified half-wing model

After applying several inclination angles of the slot, the angle of 45° was found to be the best angle of inclination from the aerodynamic performance perspective. It was the only angle to provide stable solutions on the simulations. The solution of the cases appeared not to be stable at angle of attack 20°, which appeared to be the stall angle. Table IX shows the results obtained by the baseline half-wing model at high-altitude flight case. Figures 18 and 19 show the pressure contours and velocity streamlines at mid-section of the wing at angles of attack 2°, and 19°, respectively.

TABLE IX
MODIFIED HALF-WING MODEL AT HIGH-ALTITUDE FLIGHT RESULTS

AoA (α)°	Projected area (m^2)	Lift coefficient c_l	Drag coefficient c_d
0	0.95773	-0.06527	0.12123
1	0.97611	0.10871	0.11539
2	0.98283	0.40374	0.12543
3	1.01362	0.81793	0.13865
4	1.01257	1.25160	0.16050
5	1.04666	1.65000	0.18246
6	1.08104	2.03860	0.21010
7	1.11491	2.48190	0.24081
8	1.15802	2.84070	0.27347
9	1.22348	3.05140	0.30319
10	1.28380	3.22860	0.33251
11	1.35484	3.33470	0.36087
12	1.44191	3.37280	0.38666
13	1.51148	3.42600	0.42232
14	1.59632	3.42130	0.45363
15	1.68211	3.39000	0.48658
16	1.76857	3.34070	0.51911
17	1.85501	3.27500	0.55270
18	1.94161	3.21270	0.58487
19	2.02870	3.14000	0.61799
20	2.10919	Stall	

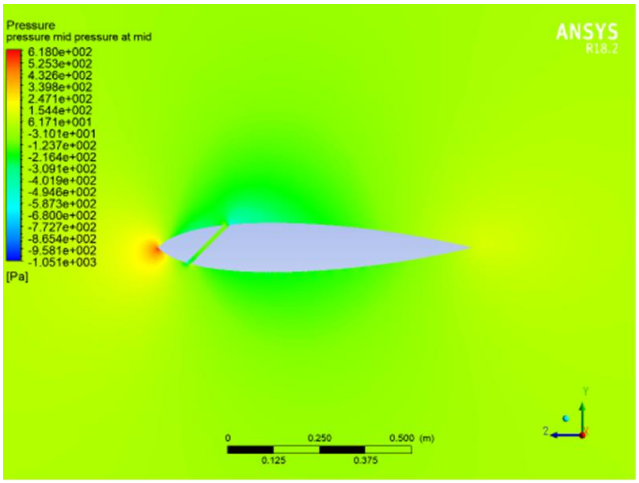

(a)

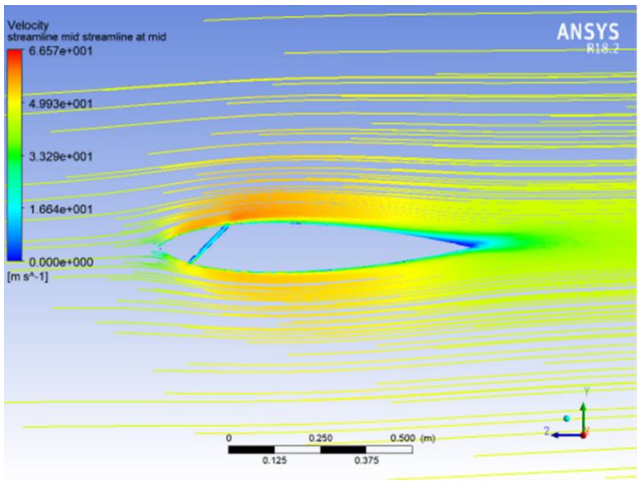

(b)

Fig. 18. Mid-section at α = 2°, (a) pressure contours (b) Velocity streamlines.

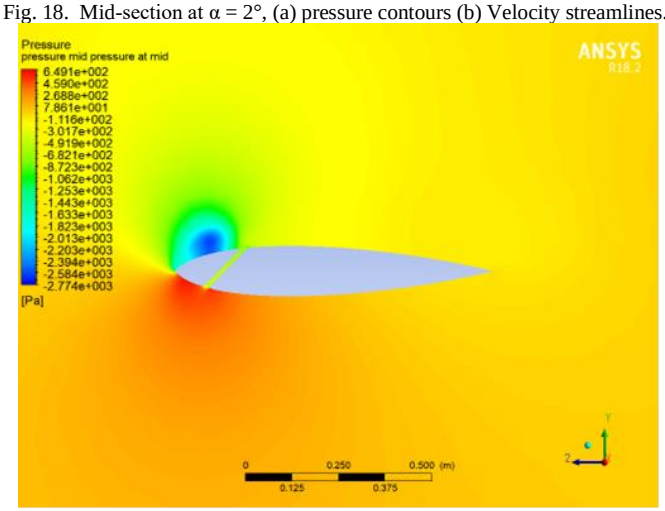

(a)

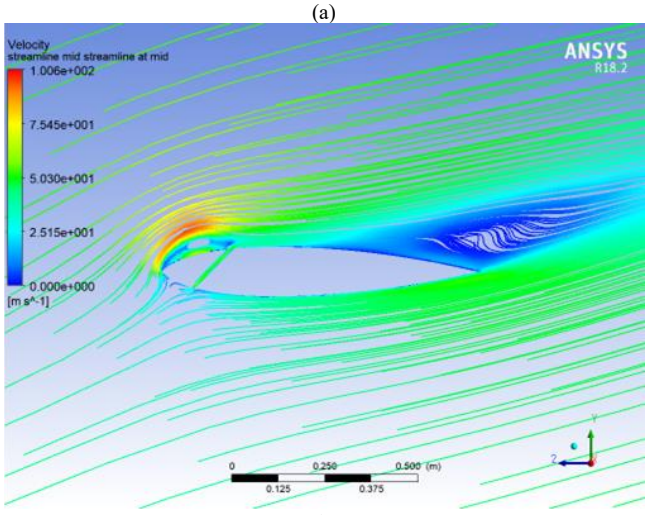

(b)

Fig. 19. Mid-section at α =13°, (a) pressure contours (b) velocity streamlines.

Baseline half-aircraft model

The solution of this case appeared not to be stable at the angle of attack 21°, which appeared to be the stall angle. Table X shows the results obtained by the baseline half-aircraft model at high altitude flight cases. Figures 20-23 show the pressure contours and velocity streamlines at plane of symmetry, and Plane of missile of the aircraft at angles of attack 2°, and 21°, respectively.

TABLE X
BASELINE HALF-AIRCRAFT MODEL AT HIGH-ALTITUDE FLIGHT RESULTS

AoA (α)°	Projected area (m^2)	Lift coefficient c_l	Drag coefficient c_d
0	1.96823	-0.0833	0.153
1	1.82	0.194	0.158
2	1.95	0.471	0.148
3	2.070029	0.708	0.143
4	1.984135	0.995	0.156
5	2.05	1.2101	0.161
6	2.180254	1.3699	0.165
7	2.2220305	1.5759	0.179
8	2.6408515	1.5511	0.170
9	2.6529775	1.7716	0.196
10	2.686658	1.9622	0.227
11	2.81861868	2.0713	0.254
12	2.908617445	2.1872	0.293
13	3.0743325	2.2376	0.329
14	3.2186075	2.2927	0.369
15	3.35650667	2.3376	0.410
16	3.455	2.3842	0.460
17	3.67	2.339	0.489
18	3.76	2.3449	0.533
19	3.96	2.2688	0.559
20	4.08	2.504	0.737
21	4.18	Stall	

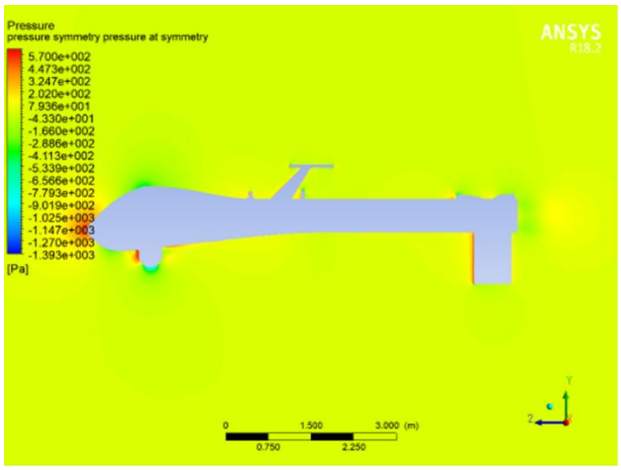

(a)

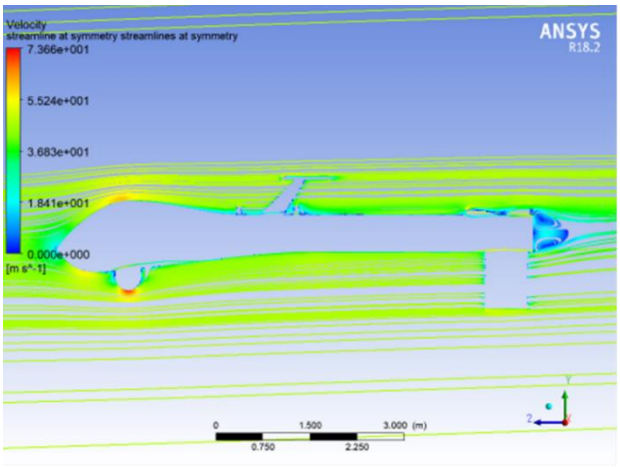

(b)

Fig. 20. Plane of symmetry at α = 2°, (a) pressure contours (b) velocity streamlines.

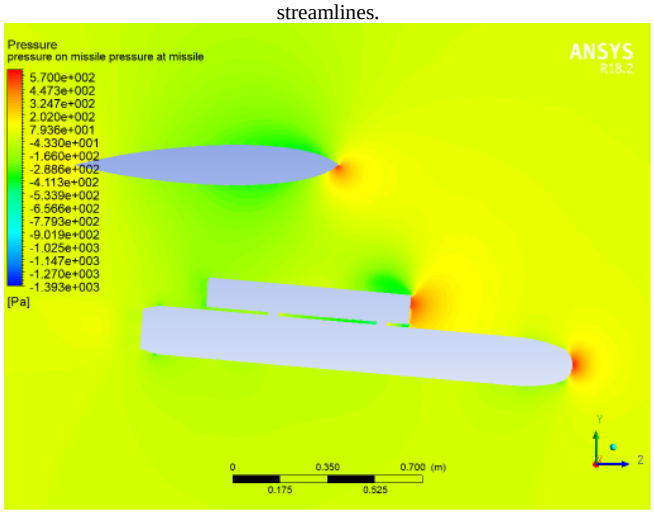

(a)

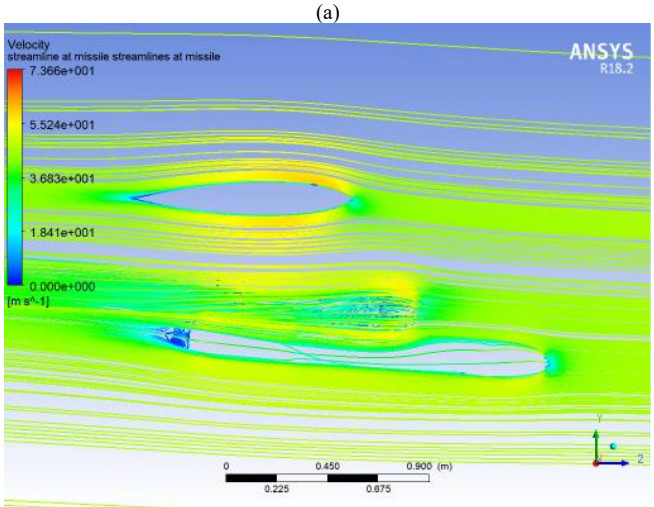

(b)

Fig. 21. Plane of missile at α = 2°, (a) pressure contours (b) velocity streamlines.

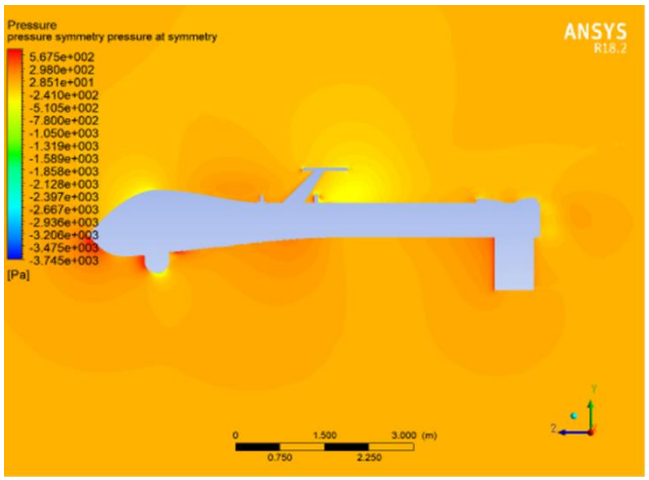

Fig. 22 (a)

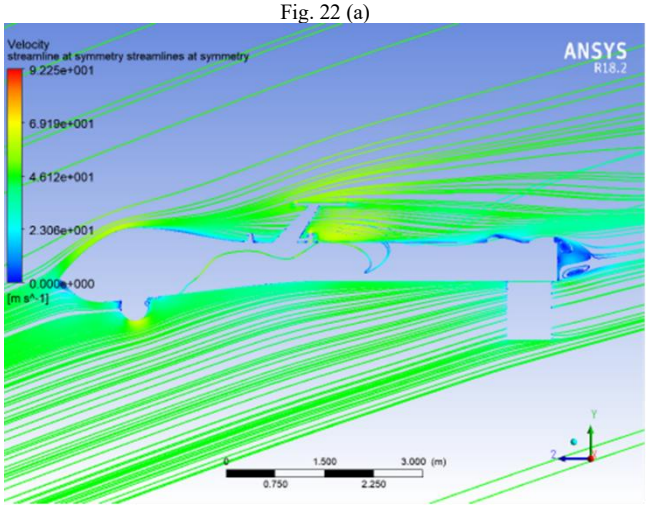

Fig. 22 (b)

Fig. 22. Plane of symmetry at α = 21°, (a) pressure contours (b) velocity streamlines.

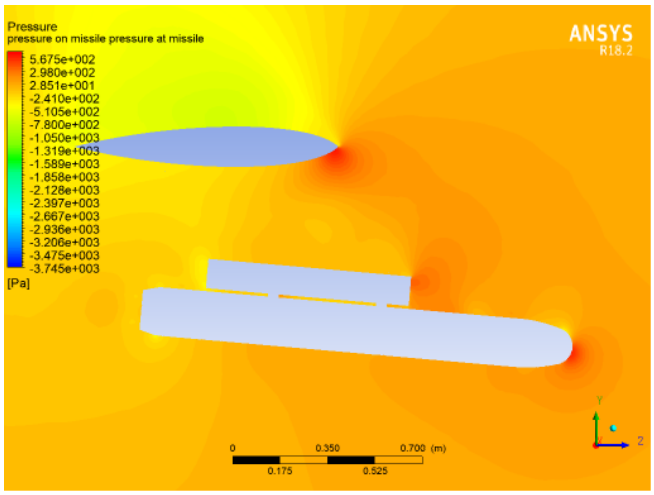

Fig. 23 (a)

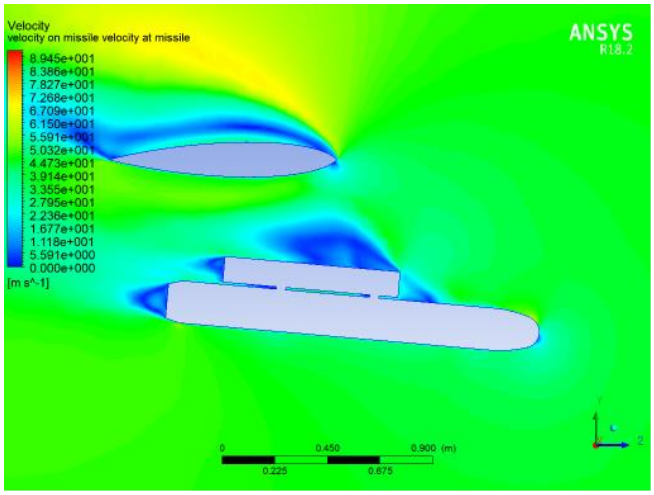

Fig. 23 (b)

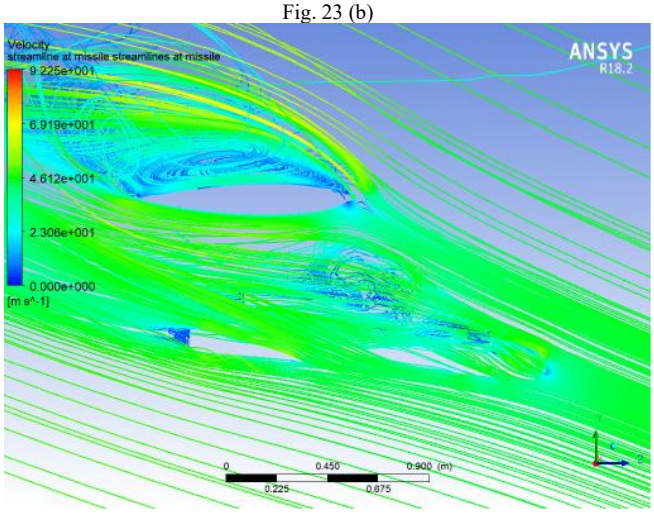

Fig. 23 (c)

Fig. 23. Plane of missile at α = 21°, (a) pressure contours (b) velocity contours (c) velocity streamlines.

Modified half-aircraft model

The solution of this case appeared not to be stable at the angle of attack 8°, which appeared to be the stall angle due to the interaction between the flow around missiles and the slot of the wing. Table XI shows the results obtained by the modified half-aircraft model at high altitude flight case. Figures 24 and 25 show the pressure contours and velocity streamlines at missile plane of the aircraft at angles of attack 2° and 8°, respectively.

TABLE XI

MODIFIED HALF-AIRCRAFT MODEL AT HIGH-ALTITUDE FLIGHT RESULTS

AoA (α)°	Projected area (m^2)	Lift coefficient c_l	Drag coefficient c_d
0	1.96823	-0.0921	0.160
1	1.82	-0.0741	0.177
2	1.95	-0.0480	0.162
3	2.070029	-0.0244	0.152
4	1.984135	-0.00623	0.159
5	2.05	0.0104	0.155
6	2.180254	0.0251	0.147
7	2.2220305	0.0378	0.146
8	2.6408515	Stall	

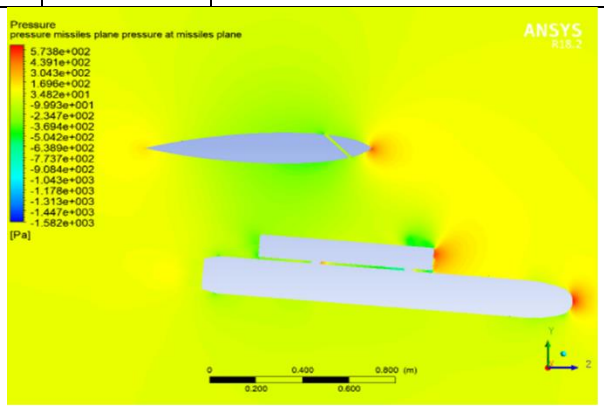

(a)

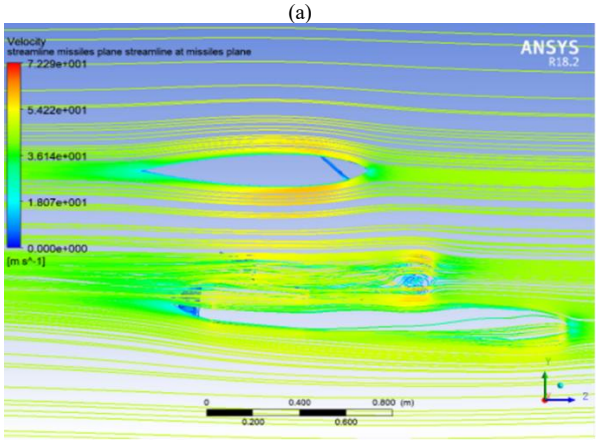

(b)

Fig. 24. Missile plane at α=2°, (a) pressure contours (b) velocity streamlines.

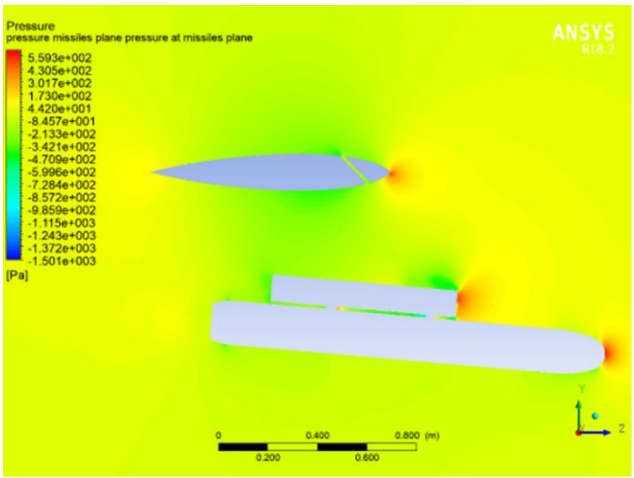

Fig. 25 (a)

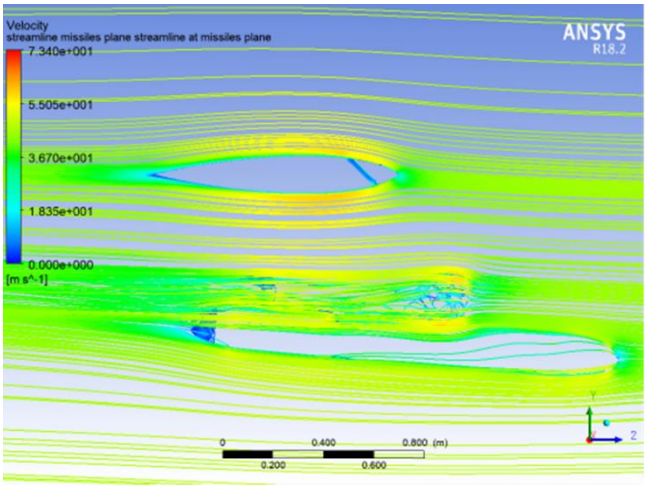

Fig. 25 (b)

Fig. 25. missile plane at α=8°, (a) pressure contours (b) velocity streamlines.

Results Analysis

Generally, the baseline wing model shows, at high-altitude cases, that the lift coefficient is higher, and the drag coefficient is lower than the modified model at the small angles of attack, Fig. 26. The advantage of the modified model appears at higher angles of attack starting of around 13°. The baseline wing shows after this angle, a severe reduction in lift coefficient and rise in drag coefficient, which is the stall point. In case of the modified wing model, the stall angle is delayed to around 19°. The reason for that is that the slot in the modified model attaches the flow to the upper surface of the wing such that the separation is delayed. Hence, the stall is delayed. This behavior of the modified model, at high angles of attack, gives an idea for controlling the slot to be open or closed. Thus, at small angles of attack, the wing slot is closed and at high angles of attack the wing slot is open, which leads to better aerodynamic performance.

As can be seen in Fig. 27, the baseline aircraft model shows that the lift coefficient is higher and drag coefficient is lower than the modified model at different angles of attack. Due to the full configuration simulation of the aircraft model with the modified wing, the advantage of the modified wing disappeared as a result of flow interaction between the weapon system of the aircraft and the slot of the modified wing. The simulations of the modified aircraft cannot be done after 8° angle of attack. The baseline aircraft without wing modifications becomes more efficient aerodynamically and stall occurs at 21° angle of attack, which is indicated by a severe reduction in lift coefficient and rise in drag coefficient.

The modified design is manufactured using Carbon fiber, laser cut wooden parts and 3D printed parts for supporting the structure. A simple control system is developed, and the manufactured model will be used for further testing.

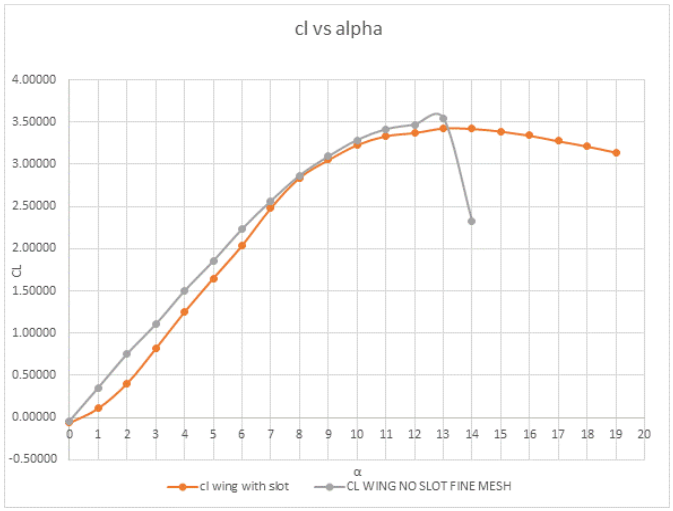

(a) (C_l-α) plot for Baseline vs Modified wing.

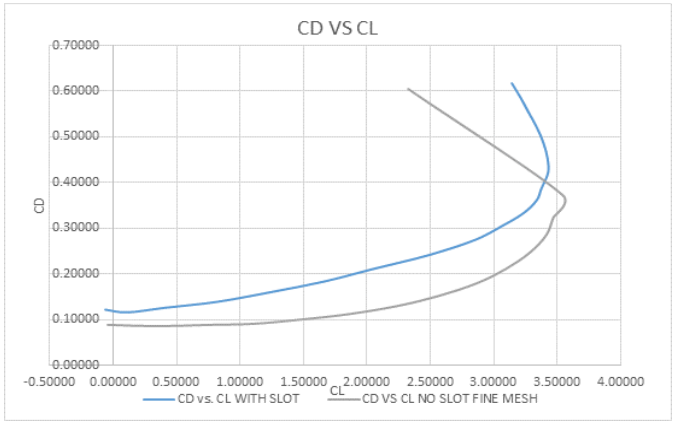

(b) (C_l-C_d) plot for Baseline vs Modified wing.

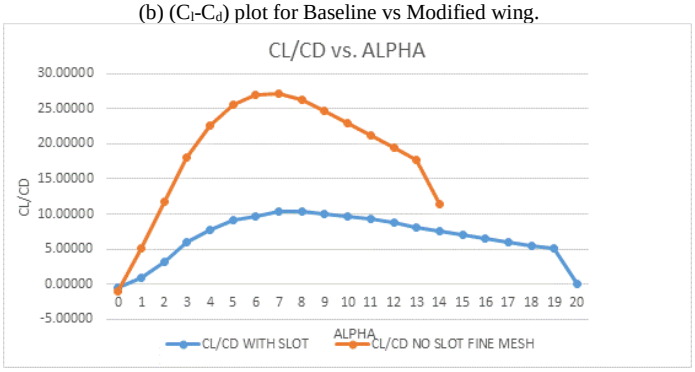

(c) (C_l/C_d- α) plot for Baseline vs Modified wing.

Fig. 26. Results of C_l and C_d for Baseline vs Modified wing case studies at high-altitude flight.

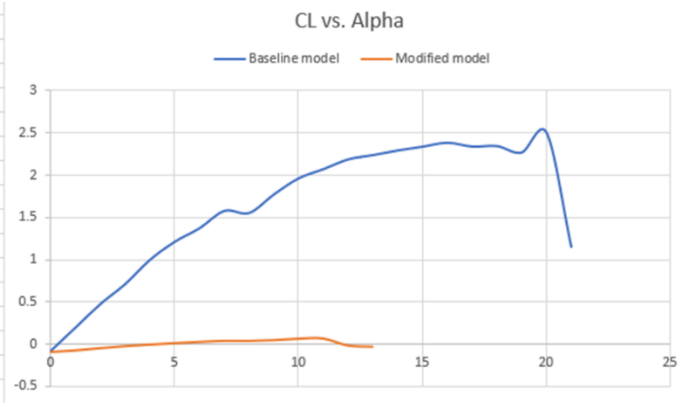

(a) (Cl-α) plot for Baseline vs Modified aircraft.

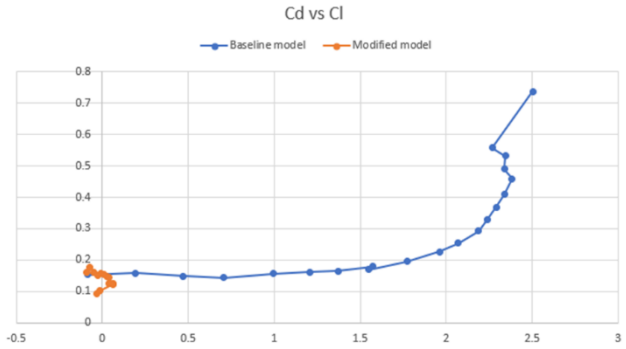

(b) (Cl-Cd) plot for Baseline vs Modified aircraft.

Fig. 29. Results of C_l and C_d for Baseline vs Modified aircraft case studies at high-altitude flight.

(a) Overall view.

(b) Top view.

Fig. 30. The present manufactured modified model.

IV. Conclusion

The baseline wing stall angle of attack is 14°. The modification applied to the wing delays the stall after 19° angle of attack. The modified and baseline wing case studies, at high-altitude flight, show that the use of either the slotted wing or baseline wing does not give the optimum design. Thus, it is required to merge their benefits together by controlling the slot opening at different angles of attack. The full configuration of baseline aircraft model case studies shows that stall is at 21°, while the modified aircraft has a bad effect due to interaction between the flow around the weapon system and the slot in the wing.

V. Nomenclature

AoA	Angle of attack
C_d	Drag coefficient
C_l	Lift coefficient
M	Mach number
S_{ij}	Strain-rate tensor
U_i	Average velocity
$\overline{u_i' u_j'}$	Reynolds stress
α	Angle of attack
ν_T	Turbulent, or eddy viscosity
ρ	Density

VI. References

[1] Gundlach, Jay, and Jay Gundlach. Designing unmanned aircraft systems: a comprehensive approach. Reston, VA: American Institute of Aeronautics and Astronautics, 2012.

[2] McGarry, Brendan (18 June 2012) Drones Most Accident-Prone U.S. Air Force Craft: BGOV Barometer Bloomberg, Archived 26 August 2013 at the Wayback Machine.

[3] Sweeten BC. CFD analysis of UAVs using VORSTAB, FLUENT, and advanced aircraft analysis software [dissertation]. Kansas: University of Kansas; 2010.

[4] Zhen TK, Zubair M, Ahamad KA. Experimental and numerical investigation of the effects of passive vortex generators on Aludra UAV performance. Chin J Aeronaut 2011, 24(5):577-83.

[5] Krishnamurthy S, Jayashankar S, Rao SV, et al. CFD analysis of an RC aircraft wing. Int J Mech Prod Eng (IJMPE) 2014, 2:63-8.

[6] Prakash Bagul, Zeeshan A. RANA, Karl W. Jenkins, La´szlo´ KO¨NO¨ZSY. Computational engineering analysis of external geometrical modifications on MQ-1 unmanned combat aerial vehicle.

[7] Vista, W. (n.d.). General atomics MQ-1 predator. Wallpapers Vista, https://vistapointe.net/general-atomics-mq-1-predator.html [Last Retrieved: June 2022].

[8] ANSYS FLUENT 12.0 User's Guide https://www.afs.enea.it/project/neptunius/docs/fluent/html/ug//main_pre.htm [Last Retrieved: June 2022].

[9] Mark Jason Thomas Loutun, Didane, D. H., Batcha, M. F. M. ., Abdullah, K. ., Mohd Ali, M. F., Mohammed, A. N. ., & Afolabi, L. O. . (2021). 2D CFD Simulation Study on the Performance of Various NACA Airfoils. CFD Letters, 13(4), 38-50. https://doi.org/10.37934/cfdl.13.4.3850 [Last Retrieved: June 2022]

[10] Mohamed, A. E., AbdelFatah, R. T., & amp; AbdelGawad, A. F. (2021, April 2). Aerodynamic Performance of Airbus BELUGA-XL for Different Cases of Natural Phenomena and using Bio-Inspired Tubercles. https://www.researchgate.net/publication/351326969_Aerodynamic_Performance_of_Airbus_BELUGA-XL_for_Different_Cases_of_Natural_Phenomena_and_using_Bio-Inspired_Tubercles. [Last Retrieved June 2022].

[11] Reynolds Number. (2019). Nasa.gov. https://www.grc.nasa.gov/www/k-12/airplane/reynolds.html [Last Retrieved June 2022].

[12] Design and Specifications. (n.d.). https://mq-1predator.weebly.com/design-and-specifications.html [Last Retrieved June 2022].

[13] Free CAD Designs, Files & 3D Models | The GrabCAD Community Library. (n.d.). Grabcad.com. https://grabcad.com/library/mq-1-predator-uav-1 [Last Retrieved June 2022].